Enhanced COD Reduction of Olefin Plant Spent Caustic Wastewater using Easily Recyclable Cu(BDC)/MgO Nanocomposites

Abstract

This study explored the photocatalytic degradation process for treating industrial spent caustic wastewater, focusing on reducing chemical oxygen demand (COD). Cu(BDC)/MgO nanocomposites were synthesized using a microwave-assisted technique, serving as efficient photocatalysts. An artificial neural network (ANN) model was established to estimate COD concentrations and optimize treatment parameters, with a target of achieving a superior COD reduction. The research aimed to minimize the hydrogen peroxide to COD ratio and optimize other factors influencing COD removal. The synthesized nanocomposites were characterized by X-ray diffraction (XRD), field emission scanning electron microscopy (FE-SEM), and energy-dispersive X-ray spectroscopy (EDS) elemental mapping. Optimal parameters for achieving a 97.55% COD removal efficiency were identified as a nanocomposite dose of 1.30 g/L, an H_2O_2/Spent caustic wastewater ratio of 1.50 ml/L, a pH of 3.0, a treatment time of 35 min, and an aeration flow rate of ٢,٥٠ L/min. Catalyst recycling studies demonstrated the exceptional recyclability and stability of the Cu(BDC)/MgO nanocomposites, showing they could be reused as catalysts even after five treatment cycles. This highlights the potential for prolonged and sustainable use of these nanocomposites in wastewater treatment processes, effectively reducing COD levels in spent caustic effluents.

Keywords: Cu(BDC)/MgO Nanocomposites, Chemical oxygen demand Spent caustic, Degradation, Petrochemical effluent, Artificial neural network

1. *Introduction*

A large amount of organic wastewater is generated from industrial activities [1], especially from petroleum and refinery operations that contain persistent pollutants [2]. Spent caustic, a complex and hazardous wastewater from gas scrubbing and petrochemical processes [3], is difficult to treat due to its high pollutant content, highly alkaline conditions (pH > 12), elevated salinity (5-12 wt% sodium), and a high sulfide content (2-3 wt%) [4]. Effective management and pre-treatment of spent caustic are crucial before conventional wastewater treatment can be applied [5]. Olefin units in the oil and gas industry use caustic substances, particularly sodium hydroxide, to remove organic sulfur compounds, hydrogen sulfide, carbon dioxide, acidic components, and other impurities from hydrocarbon streams such as natural gas and liquid petroleum gas [6, 7]. Caustic is also used to treat furnace exhaust gases, absorb CO_2, purify petroleum cuts, dehydrate hydrocarbons, and in processes like gas washing and oil sweetening [8, 9]. Additionally, it is applied for scrubbing gasoline, kerosene, and distilled oils. However, the resulting spent caustic is a hazardous and toxic industrial effluent with high alkalinity, unpleasant odor, and high concentrations of sulfide ions and volatile organic compounds [10, 11]. These properties restrict available treatment options, making conventional methods like open air, biological, and Fenton technologies less effective [12]. The treatment system design is further complicated by strict environmental policies.

Treatment methods for spent caustic are mainly categorized as biological, chemical, and thermal processes, each with drawbacks related to efficiency, cost, safety, and secondary pollution risks [13,14]. Chemical treatments, especially chemical oxidation, are the most widely used and can be divided into classical and advanced oxidation processes (AOPs). These AOPs comprise various

techniques, including Fenton oxidation, electrochemical oxidation, photo-Fenton oxidation, UV-based processes, sonolysis, nonthermal plasmas, photocatalysis, and radiolysis methods [15]. Photocatalytic degradation stands out for effectively degrading hazardous and refractory organic pollutants due to its strong oxidation ability and environmental compatibility [16]. However, its large-scale application is limited by the fast charge carrier recombination [17]. A two-step process of acid neutralization and steam stripping is used to treat spent caustic, reducing but not fully eliminating mercaptans and sulfides, which can still cause odors [18]. The effluent retains high BOD and COD due to persistent organic compounds [19], and the feedstock composition in olefin plants influences sulfur content and COD control [20]. Due to these limitations, photocatalytic degradation is proposed as a more effective method for COD removal. Conventional photocatalysts have limited efficiency due to small surface areas and dependence on UV light, resulting from their large band gaps [21]. To address these issues, new photocatalyst materials that can be activated by visible light are being explored to improve efficiency and applicability [22]. The properties of nanomaterials are closely linked to their geometric structures, making the study of structure-property relationships crucial [23]. Various nano-metal oxides, such as magnesium oxide, have attracted attention for their unique properties [24, 25]. Combining different metal oxides allows for property customization [26, 27], with MgO standing out due to its non-toxic nature, cost-effectiveness, and reusability [28, 29]. Although nano-MgO can be synthesized by several methods [30-32], its photocatalytic efficiency is limited by the poor light harvesting and fast charge recombination [33]. Current research focuses on defect engineering, carbon composites, morphology control [34], and doping with transition metals to enhance sunlight-driven activity [35-38]. The present study aims to synthesize a novel Cu(BDC)/MgO nanocomposite for efficient photocatalytic degradation of COD in petrochemical wastewater. In Cu(BDC) MOFs,

photon-absorbing organic linkers generate charge-separated states, but photocatalytic efficiency is limited by electron-hole recombination [39]. Integrating MgO with Cu(BDC) reduces this recombination, enhancing performance. Copper is preferred for MOF synthesis due to its low cost, abundance, and non-toxicity, with Cu-BDC (from copper nitrate and terephthalic acid) offering easy, eco-friendly preparation [40, 41]. Cu-BDC shows high stability in aqueous solutions across pH levels, resulting from strong coordination bonding between copper and the -COOH functional groups of BDC [42, 43]. In this work, the microwave-assisted synthesis was employed for its rapid, energy-efficient, and safe reaction conditions. To elucidate the complex, nonlinear behavior of the photocatalytic system, an ANN was utilized, offering time and cost advantages over traditional experimental designs.

2. Experimental Section

2.1. Chemicals and Instruments

All chemicals and solvents utilized in this study were procured from Sigma-Aldrich and were of analytical grade, employed as received without any subsequent purification. For pH measurement, an AL20 pH/Redox/Temperature meter (AQUALYTIC, Germany) was used. COD was measured using the LCK 014 kit (HACH company). XRD analysis was performed using a Philips instrument (model: PW ١٨٠٠) with Cu kα radiation (٤٠ kV and ٤٠ mA). The morphology of the synthesized nanocomposites was examined using a FE-SEM (Sigma, Zeiss), while EDS tests were performed through a silicon drift detector from Oxford Instruments.

2.2. Synthesis procedure

Cu(BDC)/MgO nanocomposites were synthesized using a technique involving microwave assistance [44]. Initially, a mixture of copper (II) nitrate trihydrate (1.45 g) and terephthalic acid (1 g) was combined with 75 mL of DMF and stirred at 25 °C for 10 min. Then, the solution was subjected to ultrasonic treatment for 1 minute to ensure complete dissolution. The resulting solution was then transferred to a microwave oven and exposed to a power of 700 W for a period of 8 min. The blue precipitate that formed was filtered and washed with fresh DMF on three occasions. Finally, the obtained Cu-BDC MOF was oven-dried at 220 °C for 24 h.

The nano-sized magnesium oxide (MgO) powder was prepared through a precipitation technique [45]. The aqueous magnesium nitrate hydroxide solution was prepared by dissolving 0.02 mol of $Mg(NO_3)_2.6H_2O$ in 100 mL of double distilled water. The mixture was stirred for 4 h until it became transparent. To adjust the pH to 9, ammonia was added dropwise to the solution. This resulted in the immediate formation of a precipitate. The resulting precipitate was washed repeatedly with methanol and distilled water, subsequently filtered and dried overnight in an oven maintained at ١٠٠ °C. After grinding, the dried material was subjected to calcination at ٥٠٠ ºC for three hours in a muffle furnace, yielding the final MgO nano-powder. To prepare Cu(BDC)/MgO nanocomposites, 0.5 g of the as-prepared MgO nano-powder was dispersed in a solution containing 1.45 g of copper (II) nitrate trihydrate and 1 g of terephthalic acid. After combination with 75 mL of DMF, the mixture was stirred at a fixed temperature for 15 min. Afterwards, the solution was subjected to an ultrasonic bath for 1 min to facilitate complete dissolution. Next, the solution was placed into a microwave oven and heated at 700 W for 5 min. The resulting solid precipitate was then centrifuged, washed three times with distilled, and dried at 220 °C in an oven for 24 h. Fig. 1 depicts a schematic representation of the synthesis process.

Fig. 1. Schematic of the synthesis procedure.

2.3. Treatment process

To assess the photocatalytic capabilities of Cu(BDC)/MgO nanocomposites, this photocatalyst was employed to COD reduction of spent caustic wastewater. The optimal conditions for maximum COD removal were identified experimentally. The effect of various operational factors was examined in this investigation, including the loading of the photocatalyst (g/L), H_2O_2/SCW (ml/L) the concentration of H_2O_2 (g/L), pH, operation time (min), and aeration rate (L/min). To conduct the tests, a photocatalytic reactor was utilized with a capacity of 2000 cm^3 (Fig. 2). A mechanical stirrer was present in the reactor to facilitate mixing. An air pump equipped with a sparger was used to guarantee sufficient oxygen transfer. The reaction temperature was regulated by means of coolant water recirculation through the jacket of the photocatalytic reactor. For each run, the solution volume of 1500 cm^3 was adjusted to the desired value of pH by using 0.1M H_2SO_4 and 0.1M NaOH. Then, the resulting solution was introduced into the photocatalytic reactor.

Subsequently, the stirring was initiated and a specific quantity of Cu(BDC)/MgO nanocomposites was added to attain the required concentration. To achieve maximum adsorption of the nanocomposites at equilibrium, the mixture was stirred for 20 min prior to activating the lamps. Once the lamps were turned on, both the lamps and the aeration system were activated. Following the designated reaction period, the samples were promptly collected and transferred into a flask. Sodium hydroxide solution was subsequently introduced to halt the reaction and eliminate any remaining hydrogen peroxide that could interfere with COD analysis. The samples were subjected to centrifugation at 4500 rpm for 5 min and filtered prior to measuring the COD concentration. COD analysis is widely utilized as a reliable method for quantifying the organic content present in wastewater. This technique assesses the amount of waste by determining the total oxygen required to oxidize organic substances into carbon dioxide and water. In this study, COD levels were measured using HACH's COD procedure with the aid of a COD reactor. The standard closed reflux and colorimetric techniques were applied, and sample absorbance for the COD assessment was determined using a spectrophotometer [46]. The efficiency of COD removal was calculated according to the following equation (Eq. (1)):

$$COD\ Removal\ (\%) = (COD_0 - COD_t/COD_0) \times 100 \quad (1)$$

where COD_0 corresponds to the chemical oxygen demand at the initial time, and COD_t represents the value measured at the time t. To eliminate interference from residual H_2O_2 and terminate the reaction, a sodium hydroxide solution was introduced.

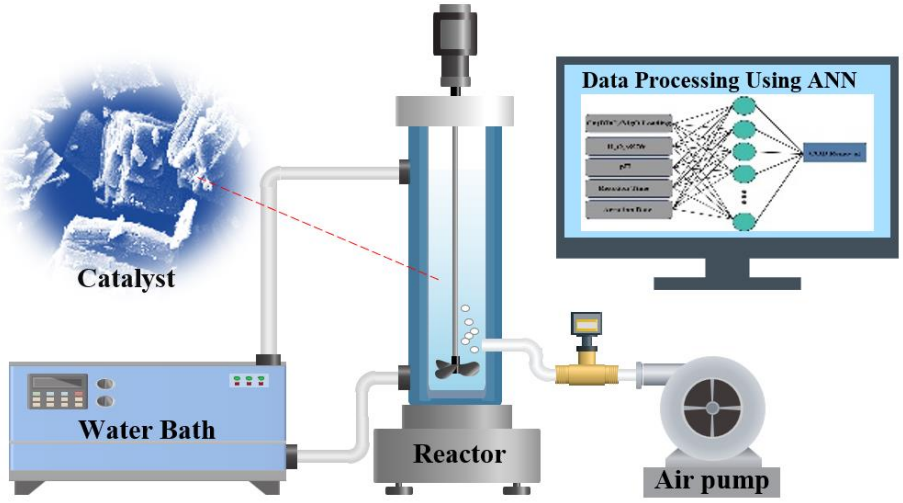

Fig. 2. Schematic of Reactor Set-up.

The raw effluent characteristics (Table 1) were collected from the neutralization stage of the Olefin unit and used as the input wastewater sample for the photocatalytic reactor.

Table. 1. The key characteristics of the used wastewater.

Characteristic	Measurement unit	Amount
COD	mg/L	1360
TDS	mg/L	285
Na_2S	wt %	0.5
pH	-	12.70
Na_2CO_3	wt %	2.5
NaOH	wt %	3
Phenols	mg/L	420

2.4. Process modeling utilizing artificial neural network (ANN)

The evaluation of process performance was conducted using ANN modeling to assess the impact of five major factors. These factors include photocatalyst loading, pH, H_2O_2/SCW, reaction time, and aeration rate. Table 2, presents the range and levels of the operational parameters.

Table. 2. Range and level of main operational parameters.

Parameter	Unit	Range
Photocatalyst dosage	g/L	0.25-2.50
H_2O_2/SCW	ml/L	1.0-3.0
pH	-	2.0-12
Aeration rate	L/min	0.5-5.0
Reaction time	min	10-60

In the present study, experimental data were used in an established ANN model, which is composed of input, hidden, and output layers. Fig. 3. illustrates the network structure based on the selected input variables. To evaluate the performance of the artificial neural network, Equations 2-5 were employed to calculate the adjusted correlation coefficient (Adjusted R^2), Mean Absolute Error (MAE), Absolute Average Deviation (AAD), and Root Mean Squared Error (RMSE).

$$R^2_{adj.} = 1 - \left[(1 - R^2)\frac{n-1}{n-K-1}\right] \quad (2)$$

$$RMSE = \sqrt{\frac{\sum_{i=1}^{n}(X_{im}-X_{ip})^2}{n}} \quad (3)$$

$$MAE = \frac{\sum_{i=1}^{n}|X_{im}-X_{ip}|}{n} \quad (4)$$

$$AAD = \left\{\frac{\sum_{i=1}^{n}|X_{im}-X_{ip}|/X_{im}}{n}\right\} \times 100 \quad (5)$$

where, K represents the number of input variables, n represents the number of data points. X_{im} and X_{ip} are the predicted and actual values, respectively for the response variable.

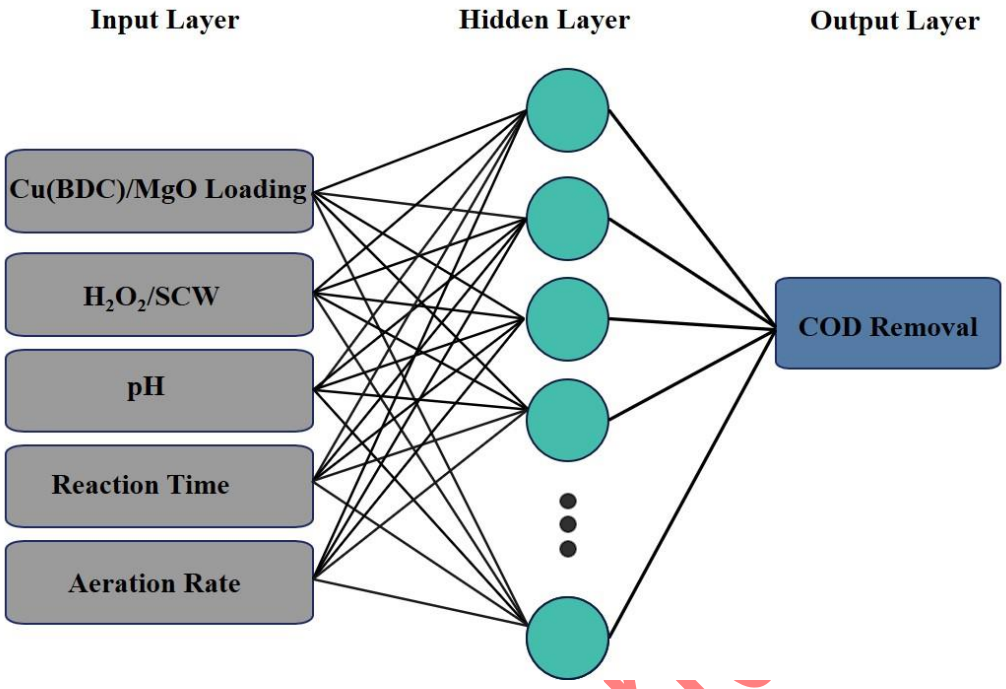

Fig. 3. Structure of the applied neural network for process modeling.

2.6. Quality assurance of the data

To ensure the results presented were reproducible and reliable, all procedures were performed in triplicate. Furthermore, the analysis of COD was conducted in triplicate for each sample, with a relative standard deviation (RSD) not exceeding 2%. This additional step helped to enhance the reliability of the findings.

3. Results and Discussion

3.1. Structure and composition of the prepared nanocomposites

Fig. 4 illustrates pronounced peaks with robust intensity for the Cu-BDC sample (XRD pattern). These peaks exhibit a remarkable resemblance to the patterns reported in earlier literature, thereby offering additional affirmation of the successful synthesis of Cu-BDC [47, 48]. The Cu(BDC) compound can be identified by its characteristic peaks at various angles (٢θ) in the X-ray diffraction pattern. As indicated in the Fig. 4, the distinctive peaks related to the synthesized Cu-BDC (CCDC no. ٦٨٧٦٩٠) are situated at ٢θ= ٩,٩°, ١٢,٠°, ١٣,٥°, ١٧,١°, ٢٠,٤°, ٢٤,٩°, ٣٤,١٥, and ٤٢,٢°. In Fig. ٤, the pattern of MgO nanoparticles is also presented. The peaks located at ٢θ values of ٣٦,٩°, ٤٢,٩°, ٦٢,٣°, ٧٤,٦°, and ٧٨,٦° within the ٢θ range can be attributed to the (١ ١ ١), (٢ ٠ 0), (220), (311), and (2 2 2) planes, respectively, of the structured MgO nanopowders. The absence of any additional peaks shows the high purity of the prepared MgO nanoparticles.

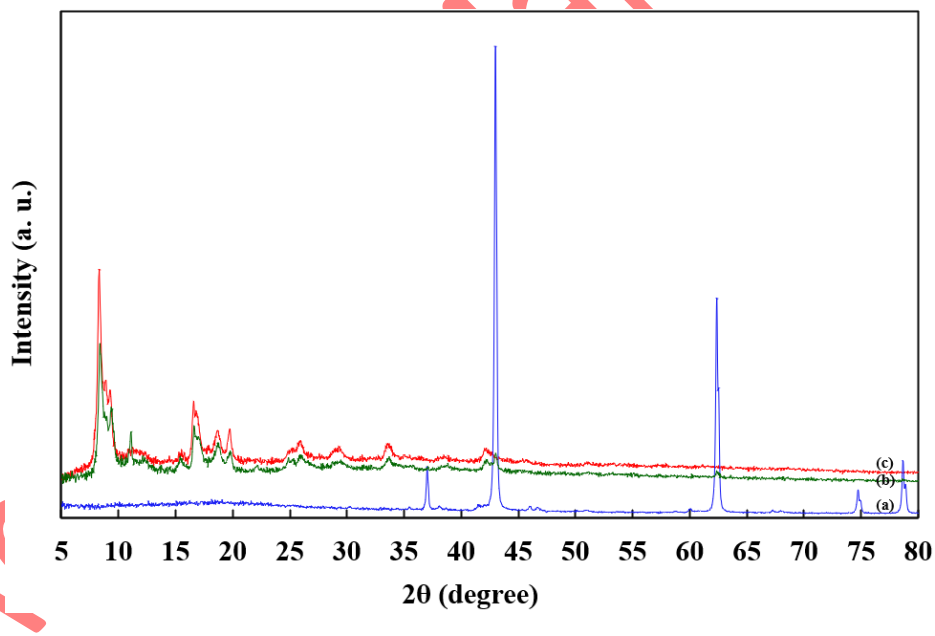

Fig. 4. XRD pattern of samples. (a): MgO nanoparticles, (b): Cu(BDC) MOF, and (c): Cu(BDC)/MgO nanocomposites.

The SEM images presented in the Fig. 5 illustrate the as-synthesized samples. The SEM image demonstrates that the Cu-BDC MOF exhibits a uniform morphology characterized by well-formed cubic shapes. These observations align with the XRD patterns obtained, providing further confirmation of the agreement between the morphology and crystal structure of the Cu-BDC MOF. In Fig. 5a, a representative SEM image of the synthesized MgO nanoparticles is displayed. Upon examining these SEM images, it becomes evident that the surface morphologies of the nanoparticles appear as assemblies, with each assembly composed of round-shaped nanoparticles.

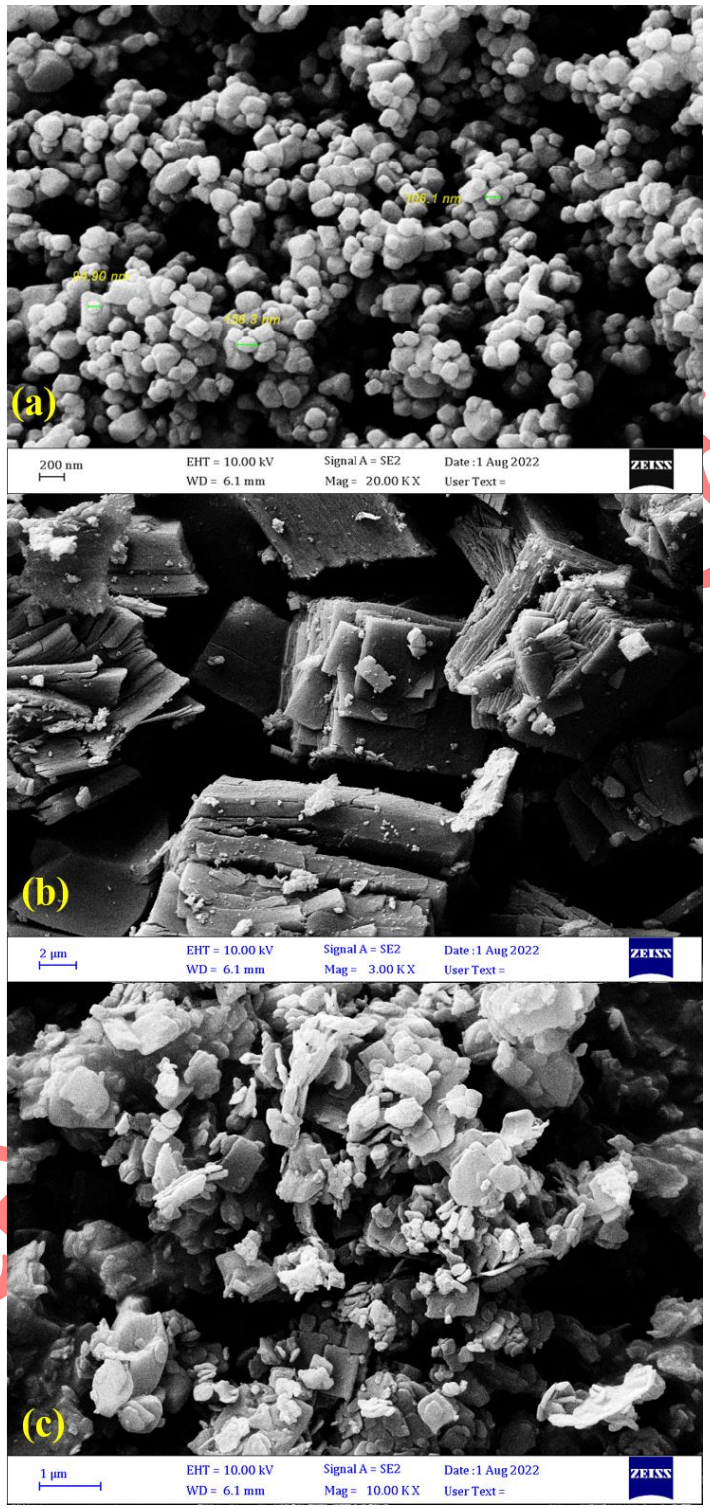

Fig. 5. FE-SEM images. (a): MgO nanoparticles, (b): Cu(BDC) MOF , and (c): Cu(BDC)/MgO nanocomposites.

In the Fig. 6 (a-c), the EDS analyses of the materials are compared. Findings indicate that the as-prepared composite exhibits the presence of atoms characteristic of Cu(BDC), as expected. However, in addition to these atoms, the presence of Mg atoms is also observed. The detection of C, Cu, and O atoms can be ascribed to the Cu-BDC MOF components in the structure of the Cu(BDC)/MgO nanocomposites. The observation of Mg atoms further confirms the stabilization of MgO nanoparticles on the Cu(BDC)/MgO nanocomposites. In the Fig. 6 (e-g), the elemental mapping analysis of the Cu(BDC)/MgO nanocomposites is presented. The results demonstrate that the MgO nanoparticles exhibit a high dispersion throughout the sample, indicating that the MgO nanoparticles have been uniformly stabilized on the Cu(BDC)/MgO nanocomposites. This observation suggests that the synthesis method employed has successfully achieved a uniform distribution of MgO nanoparticles within the Cu(BDC)/MgO nanocomposites.

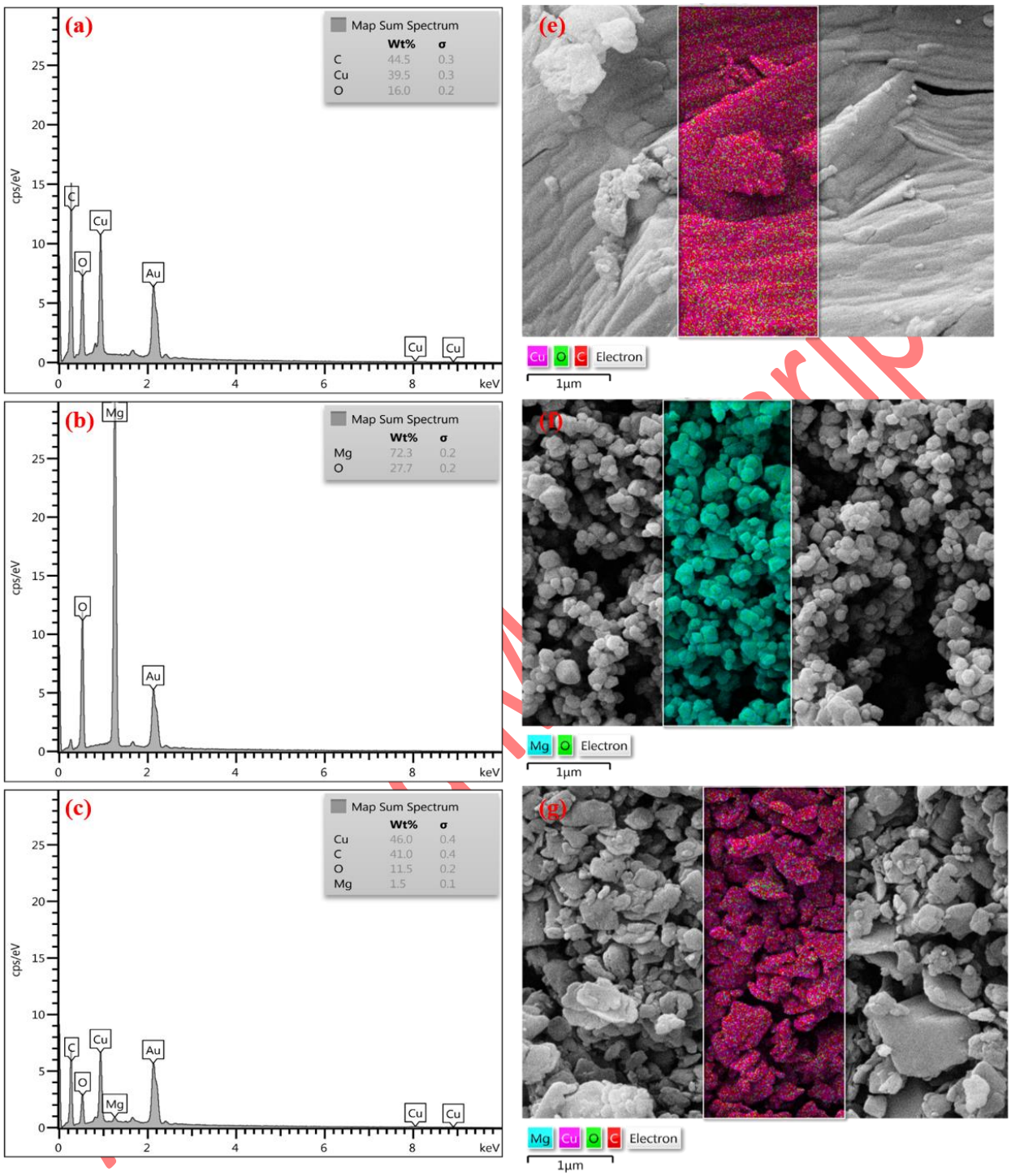

Fig. 6. EDS analysis: Cu(BDC) MOF (a), MgO nanoparticles (b), and Cu(BDC)/MgO nanocomposites (c). Elemental mapping analysis: Cu(BDC) MOF (e), MgO nanoparticles (f), and Cu(BDC)/MgO nanocomposites (g).

N_2 physisorption analysis was applied to evaluate the textural properties (i.e., surface area and porosity) of the Cu(BDC) MOF, MgO nanoparticles, and Cu(BDC)/MgO nanocomposite. The surface area to volume ratio has a crucial role in the adsorption properties of prepared nanocomposite. Cu(BDC)/MgO nanocomposites follows a Type III isotherm, as per the Brunauer-Deming-Deming-Teller classification. As shown in Fig. 7a, total pore volume of Cu(BDC) MOF, MgO nanoparticles, and Cu(BDC)/MgO samples are equal to 0.184, 0.095 and 0.277 cm^3g^{-1} the total surface area of Cu(BDC) MOF, MgO nanoparticles, and Cu(BDC)/MgO samples are 22.9, 13.3 and 189.8 m^2g^{-1} (Fig. 7b).

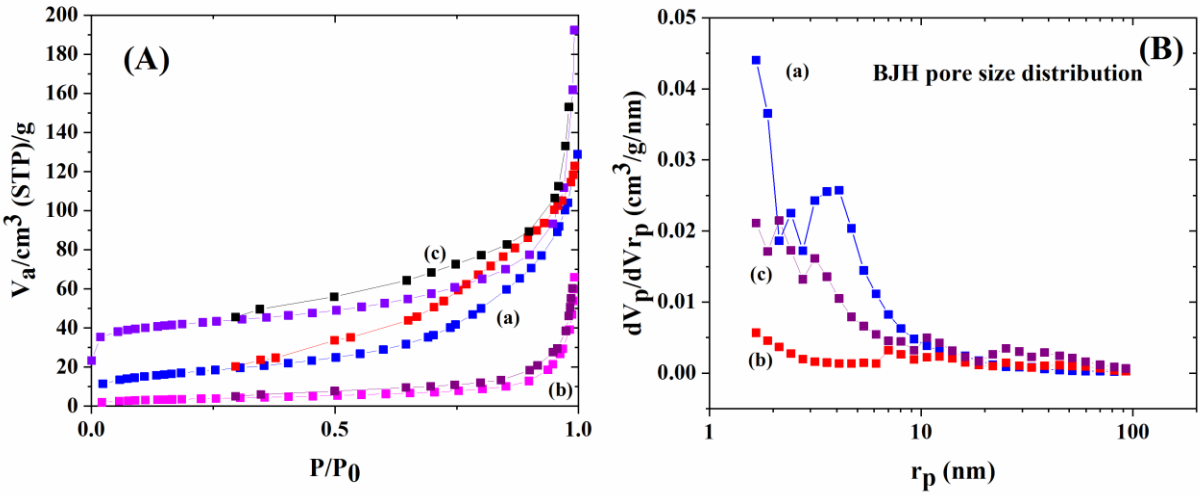

Fig. 7. Nitrogen adsorption-desorption isotherms (A) and the corresponding pore size distributions (B) of as-prepared samples

3.2. The effects of operational parameters on COD reduction

To assess the photocatalytic degradation capabilities of Cu (BDC)/MgO nanocomposites, this catalyst was applied to reduce the chemical oxygen demand (COD) in spent caustic wastewater.

The study systematically examined the effects of five variables including pH, nanocomposite dosage (g/L), aeration rate (L/min), time (min), and H_2O_2/wastewater ratio (ml/L) on reduction efficiency. Among these, pH plays a crucial role in photocatalytic reactions. Typically, such processes demonstrate greater effectiveness under acidic conditions. When the pH increases at low oxidant concentrations, a decline in process efficiency is observed, suggesting an inverse relationship between pH and oxidant levels. Additionally, raising the photocatalyst concentration often requires a corresponding increase in pH to prevent particle aggregation.

The formation of hydroxyl radicals is mainly facilitated by the interaction of photogenerated holes with H_2O molecules or OH^-. When other sources for hydroxyl radical production (e.g., hydroperoxyl radicals), are insufficient, enhancing the photocatalyst dosage can compensate for this deficiency. However, in alkaline conditions, the adsorption of contaminants onto the catalyst surface diminishes, which in turn lowers the degradation rate. Investigating the effect of pH within the range of 2.0 to 12 revealed that optimal COD reduction occurs at a pH of 3.0 (Fig. 8a).

The impact of photocatalyst dosage was also explored (Fig. 8b). Elevating the amount of photocatalyst increases the number of active sites available for electron-hole pair generation. These sites facilitate the formation of free electrons, which reduce molecular oxygen to superoxide radicals (O_2^-). The positive holes oxidize H_2O to produce hydroxyl radicals ($^{\bullet}OH$). As highly reactive oxidants, hydroxyl radicals can mineralize even persistent organic pollutants. Therefore, increasing the catalyst concentration enhances free radical production, thereby accelerating oxidation reactions and improving COD reduction efficiency.

In AOPs, H_2O_2 serves as a strong oxidant. Higher concentrations of hydrogen peroxide result in more molecules per unit volume, and under irradiation with a photocatalyst, it decomposes to form additional hydroxyl radicals. The elevated presence of these radicals further promotes the

oxidation of various organic contaminants in wastewater, leading to more rapid reductions in COD (Fig. 8c).

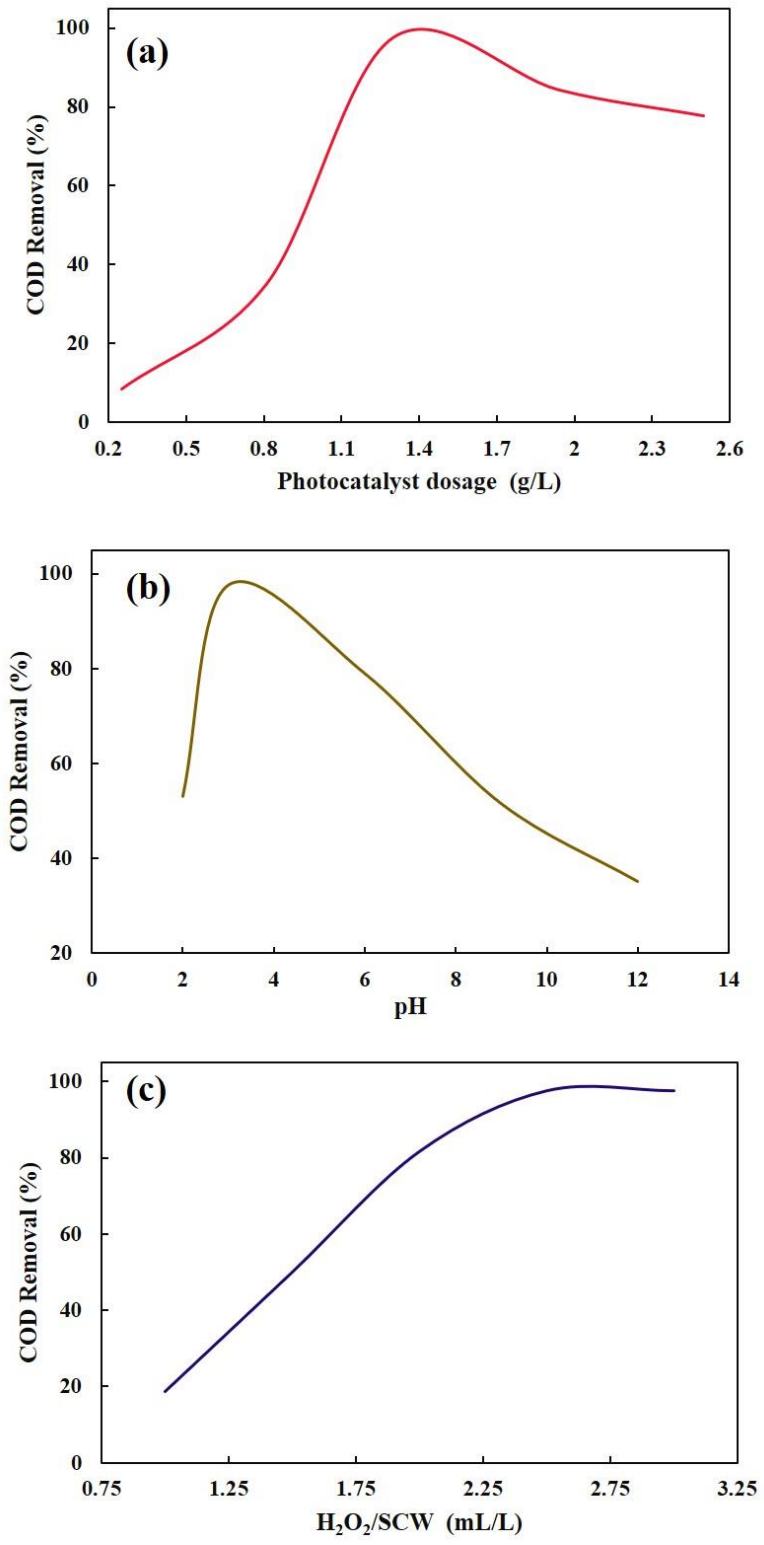

Fig. 8. The effects of operational parameters on COD reduction. (a): pH, (b): photocatalyst loading (g/L), and (c): H_2O_2/SCW.

The study also highlights the importance of optimizing aeration rates as a significant factor in designing and operating advanced oxidation water treatment systems (Fig. 9a). Enhanced aeration improves mixing and facilitates better mass transfer between oxygen and catalyst particles, which increases free radical generation and results in greater COD reduction in treated effluent. Furthermore, data indicate that extending irradiation time in photocatalytic processes directly boosts the removal efficiency of organic pollutants. Longer exposure allows more photons to reach the catalyst surface, generating additional electron-hole pairs that can participate in oxidation reactions with contaminants (Fig. 9b). This increase in both direct and indirect oxidation events with prolonged irradiation ultimately leads to improved pollutant removal outcomes. Collectively, these findings offer valuable insights for developing more efficient and cost-effective wastewater treatment technologies based on advanced oxidation processes.

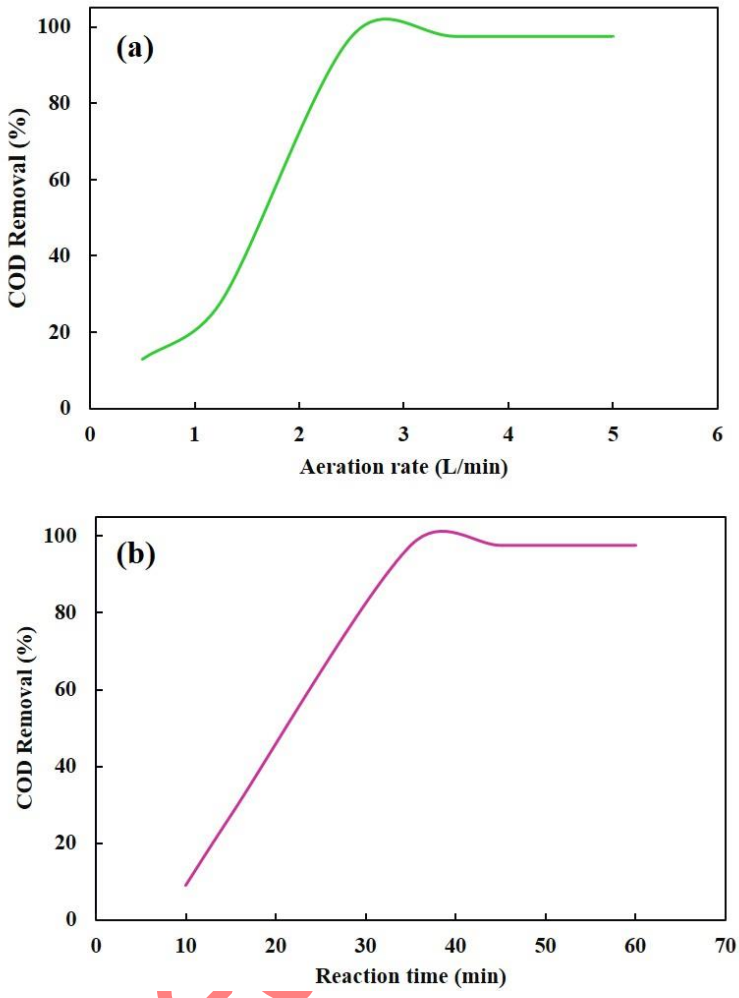

Fig. 9. The effects of operational parameters on COD reduction. (a): Aeration rate (L/min), and (b): Reaction time (min).

3.3. Degradation mechanism

Photocatalytic processes primarily proceed through two main mechanisms. The first involves the utilization of hydroxyl or water groups located on the photocatalyst surface, while the second mechanism entails direct oxidation occurring within the catalyst's cavities. When Cu(BDC)/MgO nanocomposites are exposed to light, electron-hole pairs are generated on the catalyst surface. The resulting holes associate with H_2O or hydroxyl groups, leading to the formation of hydroxyl

radicals capable of degrading organic pollutants. The sequence of reactions can be described as follows:

Cu(BDC)/MgO NCs +*hv* (*energy from light*) → e^- + h^+ (٦)

e^- +O_2→O^-_2 • (superoxide - radical) (٧)

The photogenerated electrons reduce oxygen molecules to form superoxide and hydroperoxide radical anions, which subsequently convert into hydrogen peroxide and water. Hydrogen peroxide can further undergo photolysis to yield additional hydroxyl radicals:

H_2O_2 + *hv* → ٢ OH (٨)

$h^+ + H_2O \rightarrow H^+ + OH\bullet$ (٩)

The elimination of sulphides is attributed both to their thermal decomposition at elevated temperatures and to their direct reaction with hydrogen peroxide, as represented by the following equations:

٢H_2O_2 → ٢H_2O + O_2 (١٠)

$S^{2-} + 4H_2O_2 \rightarrow SO_4^{2-} + H_2O$ (١١)

The breakdown of hydrogen peroxide may release oxygen, which can further facilitate the oxidation of sulphides. During this process, sulphidic intermediates such as thiosulphates, sulphites, and sulphates may form. Additionally, phenolic intermediates including hydroquinone, p-benzoquinone, and catechol have been detected in lower concentrations relative to organic acids [49].

The photocatalytic method proves effective for the degradation of organic contaminants. In this investigation, it achieved an 82.10% decrease in phenolic substances and a 97.55% reduction in

the COD of wastewater. Additionally, a 4.5% decrease in sulfide compounds was observed, which is probably attributable to the adsorption of these pollutants onto the catalyst surface. Inorganic ions, including Na^+ originating from Na_2S, Na_2CO_3, and NaOH, remain mostly unchanged since they do not undergo oxidation. The total dissolved solids (TDS) exhibit minimal decrease—generally less than ١٠٪—because the treatment primarily targets organic compounds rather than inorganic salts.

3.4. The process of modeling and optimizing using ANN

To identify the most favorable experimental conditions with the ANN model, a total of 26 experiments were conducted based on a systematic experimental design, which was developed after selecting suitable intervals for the independent variables. The investigated parameters comprised photocatalyst concentration (٠٫٢٥–٢٫٥٠ g/L), H_2O_2/SCW ratio (١٫٠–٣٫٠ ml/L), pH level (٢٫٠–١٢), aeration rate (٠٫٥–٥٫٠ L/min), and reaction duration (١٠–٦٠ min). The ANN-based process model was constructed using the Single Layer Perceptron (SLP) architecture. The SLP network consisted of five input nodes, representing the loading of the photocatalyst, H_2O_2/SCW, pH, reaction time, and aeration rate. Additionally, there was a single output node, which indicated the COD removal achieved during the process. To train the network, a feedforward approach was utilized, where an input training pattern was passed through the network. In a feedforward neural network, each neuron in a layer is connected to all neurons in the adjacent layer. The training process employed the Trainbr function, which is responsible for updating the weights and biases using the Levenberg-Marquardt (LM) optimization algorithm. LM minimizes a joint function of squared errors and weights, aiming to find the optimal solution that enables the network to generalize well. This approach is known as Bayesian regularization. In this study, various numbers

of neurons ranging were examined in the hidden layer of the ANN. The optimal number of neurons was determined by evaluating the correlation coefficient and the minimum Mean Squared Error (MSE) of the overall data. Fig. 10. illustrates the results. To ensure the reliability of the results, three separate runs were conducted for each network structure. Each run utilized different random values for the initial weights of the neural network. This approach helps to account for any potential bias or variability introduced by the initial weight values.

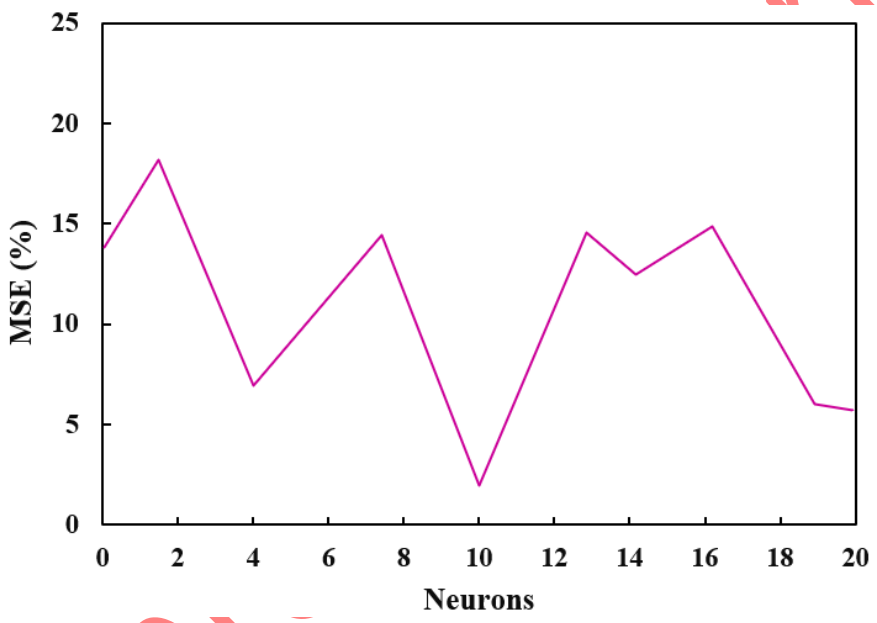

Fig. 10. The relation between MSE (%) and the number of neurons in the hidden layer.

In the Table 3, the statistical values of the ANN model are presented, including correlation coefficients, AAD, RMS, and MAE. A good model is characterized by R^2 being close to 1.0 and in good agreement with R^2_{adj}. A high R^2 value indicates a strong linear relationship. RMS should be close to zero, indicating the good agreement between the ANN model estimates and the experimental values. A small AAD between the observed and predicted values indicates a high degree of correlation between the model's estimations and the actual data. Higher values of AAD

and RMS suggest larger deviations in the estimation. It is worth noting that in the ANN model, large values of R^2 and R^2_{adj}, as well as small differences between them, indicate the accuracy of the model in predicting the desired outcome.

Table. 3. ANN model examination.

Model Factor	Value
R^2	0.9912
R^2_{adj}	0.9983
AAD	0.2966
MAE	0.2095
RMS	0.2240

3.5. Catalytic stability

The practical application of a catalyst relies significantly on its recyclability and stability. The stability of the photocatalyst was assessed through cycling experiments, which investigated its performance following multiple photocatalytic degradation processes. Fig. 11. demonstrates that even after six cycles of photocatalytic COD removal in caustic petrochemical wastewater, the Cu(BDC)/MgO nanocomposites sample exhibited remarkable stability, as it was able to maintain an 86% removal rate.

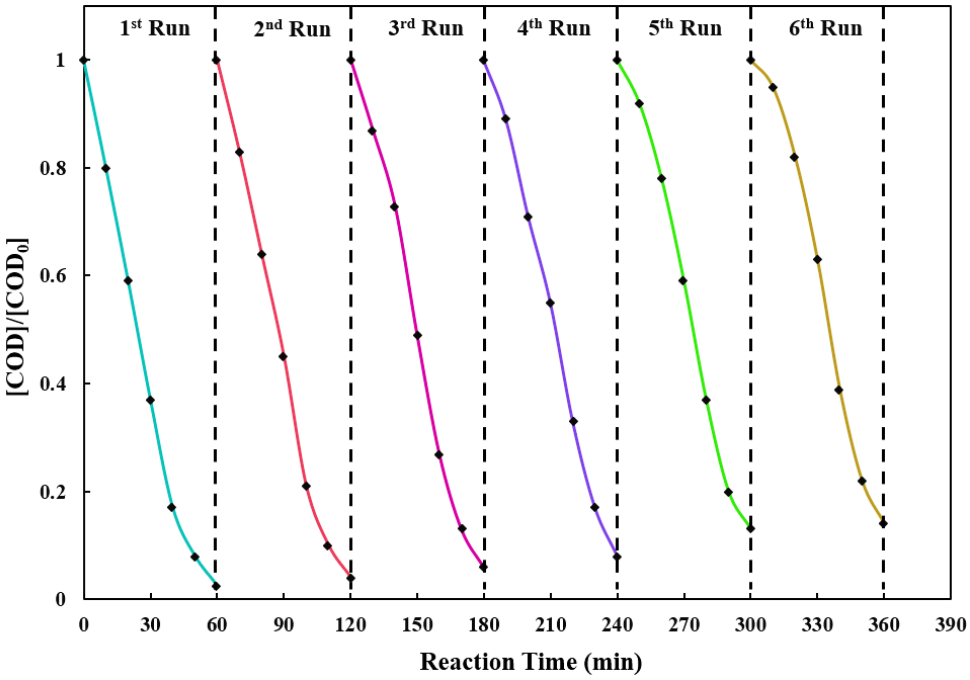

Fig. 11. Reusability of Cu(BDC)/MgO nanocomposites toward photocatalytic degradation of SCW.

3.6. Comparison of the activity of Cu(BDC)/MgO nanocomposites with some reported catalysts

The COD reduction performance of the developed system was compared with literature values, as shown in Table 4. The results in the table demonstrated that the proposed system effectively promotes the COD reduction, with the least time requirement.

Table. 4. Comparison of different treatment systems performance.

System/Process	Time (min)	COD Removal (%)
Photocatalytic degradation [18]	90	77.3%
Membrane system [42]	480	93.71%
Neutralization [5]	60	88%
Fenton process [5]	60	96.5%
Electro-photo-Fenton [43]	80	97%
This work	35	97.55%

4. Conclusions

In summary, the Cu(BDC)/MgO nanocomposites were prepared by microwave-assisted technique. The materials were characterized by XRD, FE-SEM, EDS, and elemental mapping techniques to analyze their structural, morphological, and elemental properties. The ANN-based models for prediction of COD concentrations in the spent caustic effluent were formed applying a three-layered algorithm ANN towards assessing the performance of a wastewater treatment. The fabricated nanocomposites demonstrated a high level of photocatalytic activity in reducing the COD of spent caustic. The optimal conditions for achieving the maximum COD removal (97.55%) were determined to be a photocatalyst loading of 1.30 g/L, H_2O_2/ SCW of 1.50 ml/L, pH of 3.0, time of 35 min, and aeration rate of 2.50 L/min. Furthermore, a remarkable degree of concordance was observed between the experimental data and the values obtained from the ANN model at the optimized conditions.

Nomenclature

AAD	Absolute Average Deviation
ANN	Artificial neural network
AOPs	Advanced Oxidation Processes
BET	Brunauer-Emmett-Teller
BOD	Biological Oxygen Demand
COD	Chemical Oxygen Demand
DRS	Diffuse Reflectance Spectroscopy
EDX	Energy Dispersive X- Ray
FE- SEM	Field Emission Scanning Electron Microscopy
FTIR	Fourier Transform Infrared Spectroscopy
LM	Levenberg-Marquardt
MAE	Mean Absolute Error
MgO	Magnesium Oxide
MSE	Mean Squared Error
RMSE	Root Mean Squared Error
RSD	Relative Standard Deviation
SCW	Spent Caustic Wastewater
SLP	Single Layer Perceptron
WAO	Wet Air Oxidation
WWTF	Wastewater Treatment Facility
XRD	X-Ray Diffraction

Declaration of Competing Interest

The authors affirm that they have no known competing financial interests or personal relationships that could have potentially influenced the work presented in this paper.

Acknowledgment

The authors express their gratitude to the Research Council of Yasouj University for providing financial support for this research. The authors also extend their appreciation to the Gachsaran Petrochemical Complex (Olefin Plant) for their valuable cooperation in facilitating this project.

References

[1] Liu J, Jiang L, Zhang H, Yao H, Chai J, Wang J, Fang D, Zhang Z, Tie M. Construction of high-proportion dual bismuth-based Z-scheme Bi_3O_4Cl/Bi_2MoO_6 photocatalytic system via in-situ growth of Bi_2MoO_6 on Bi_3O_4Cl for enhanced photocatalytic degradation of organic pollutants. Journal of Alloys and Compounds. 2023 Sep 15;956:170375. https://doi.org/10.1016/j.jallcom.2023.170375

[2] Li J, Wang Q, Liang J, Li H, Guo S, El-Din MG, Chen C. An enhanced disintegration using refinery spent caustic for anaerobic digestion of refinery waste activated sludge. Journal of Environmental Management. 2021 Apr 15;284:112022. https://doi.org/10.1016/j.jenvman.2021.112022

[3] Delnavaz M, Khoshvaght H, Sadeghi A, Ghasemipanah K, Aliabadi MH. Experimental, statistical and financial analysis of the treatment of organic contaminants in naphthenic spent caustic soda using electrocoagulation process modified by carbon nanotubes. Journal of Cleaner Production. 2021 Dec 10;327:129515. https://doi.org/10.1016/j.jclepro.2021.129515

[4] Hashemi SR, Heydarinasab A, Amoozegar MA. Modified biological treatment of spent caustic effluent from liquefied petroleum gas plants. Chemical Engineering & Technology. 2020 Feb;43(2):380-5. https://doi.org/10.1002/ceat.201900368

[5] Hawari A, Ramadan H, Abu-Reesh I, Ouederni M. A comparative study of the treatment of ethylene plant spent caustic by neutralization and classical and advanced oxidation. Journal of environmental management. 2015 Mar 15;151:105-12. https://doi.org/10.1016/j.jenvman.2014.12.038

[6] Zhang X, Liu T, Zhang Y, Cai Z, Wan Q. Co-operative harmless treatment and neutralization utilization process research of LPG spent caustic coupled chloroaluminate ionic liquid spent catalysts. Journal of Water Process Engineering. 2023 Apr 1;52:103507. https://doi.org/10.1016/j.jwpe.2023.103507

[7] Alipour Z, Azari A. COD removal from industrial spent caustic wastewater: A review. Journal of environmental chemical engineering. 2020 Jun 1;8(3):103678. https://doi.org/10.1016/j.jece.2020.103678

[8] González C, Pariente MI, Molina R, Espina LG, Masa MO, Bernal V, Melero JA, Martinez F. Increasing biodegradability of a real amine-contaminated spent caustic problematic stream through WAO and CWAO oxidation using a high specific surface catalyst from petcoke. Chemical Engineering Journal. 2023 Mar 15;460:141692. https://doi.org/10.1016/j.cej.2023.141692

[9] Ntagia E, Fiset E, Hong LT, Vaiopoulou E, Rabaey K. Electrochemical treatment of industrial sulfidic spent caustic streams for sulfide removal and caustic recovery. Journal of Hazardous Materials. 2020 Apr 15;388:121770. https://doi.org/10.1016/j.jhazmat.2019.121770

[10] Rita AI, Rodrigues CS, Santos M, Sanches S, Madeira LM. Comparison of different strategies to treat challenging refinery spent caustic effluents. Separation and purification technology. 2020 Dec 15;253:117482. https://doi.org/10.1016/j.seppur.2020.117482

[١١] Fernandes A, Makoś P, Wang Z, Boczkaj G. Synergistic effect of $TiO_٢$ photocatalytic advanced oxidation processes in the treatment of refinery effluents. Chemical Engineering Journal. 2020 Jul 1;391:123488. https://doi.org/10.1016/j.cej.2019.123488

[12] Gholami A, Mousavi SB, Heris SZ, Mohammadpourfard M. Highly efficient treatment of petrochemical spent caustic effluent via electro-Fenton process for COD and TOC removal: optimization

and experimental. Biomass Conversion and Biorefinery. 2024 Aug;14(15):17481-97. https://doi.org/10.1007/s13399-023-03772-2

[13] Davarnejad R, Bakhshandeh M. Olefin plant spent caustic wastewater treatment using electro-Fenton technique. Egyptian journal of petroleum. 2018 Dec 1;27(4):573-81. https://doi.org/10.1016/j.ejpe.2017.08.008

[14] Dong C, Fang W, Yi Q, Zhang J. A comprehensive review on reactive oxygen species (ROS) in advanced oxidation processes (AOPs). Chemosphere. 2022 Dec 1;308:136205. https://doi.org/10.1016/j.chemosphere.2022.136205

[15] Hua X, Chen H, Rong C, Addison F, Dong D, Qu J, Liang D, Guo Z, Zheng N, Liu H. Visible-light-driven photocatalytic degradation of tetracycline hydrochloride by Z-scheme Ag_3PO_4/1T@ 2H-MoS_2 heterojunction: degradation mechanism, toxicity assessment, and potential applications. Journal of Hazardous Materials. 2023 Apr 15;448:130951. https://doi.org/10.1016/j.jhazmat.2023.130951

[16] Zhao Y, Chang L, Li Y, He W, Liu K, Cui M, Hameed MU, Xie J. High-gravity photocatalytic degradation of tetracycline hydrochloride under simulated sunlight. Journal of Water Process Engineering. 2023 Jul 1;53:103753. https://doi.org/10.1016/j.jwpe.2023.103753

[17] Wei Y, Zhao J, Liu Z, Zhang L, Cui Q, Wang H. Study on wet oxidation process and mechanism for ethylene spent caustic. Environmental Technology. 2022 Jul 29;43(17):2637-46. https://doi.org/10.1080/09593330.2021.1892200

[18] Ahmadpour A, Asl AH, Fallah N. Synthesis and photocatalytic studies of TiO_2-clinoptilolite on spent caustic wastewater treatment. Particulate Science and Technology. 2018 Oct 3;36(7):791-8. https://doi.org/10.1080/02726351.2017.1302534

[19] Sarkodie B, Amesimeku J, Frimpong C, Howard EK, Feng Q, Xu Z. Photocatalytic degradation of dyes by novel electrospun nanofibers: a review. Chemosphere. 2023 Feb 1;313:137654. https://doi.org/10.1016/j.chemosphere.2022.137654

[20] Xu P, Ding C, Li Z, Yu R, Cui H, Gao S. Photocatalytic degradation of air pollutant by modified nano titanium oxide (TiO_2) in a fluidized bed photoreactor: Optimizing and kinetic modeling. Chemosphere. 2023 Apr 1;319:137995. https://doi.org/10.1016/j.chemosphere.2023.137995

[21] AlSalhi MS, Devanesan S, Asemi NN, Aldawsari M. Construction of SnO_2/CuO/rGO nanocomposites for photocatalytic degradation of organic pollutants and antibacterial applications. Environmental Research. 2023 Apr 1;222:115370. https://doi.org/10.1016/j.envres.2023.115370

[22] Fouda A, Hassan SE, Saied E, Hamza MF. Photocatalytic degradation of real textile and tannery effluent using biosynthesized magnesium oxide nanoparticles (MgO-NPs), heavy metal adsorption, phytotoxicity, and antimicrobial activity. Journal of Environmental Chemical Engineering. 2021 Aug 1;9(4):105346. https://doi.org/10.1016/j.jece.2021.105346

[23] Zhu Z, Xia H, Li H. Boosting photocatalytic degradation efficiency of tetracycline by a visible-light-activated $NiMoO_4$/g-C_3N_4 heterojunction photocatalyst in the water environment. Solid State Sciences. 2023 May 1;139:107164. https://doi.org/10.1016/j.solidstatesciences.2023.107164

[24] Chandrasekar M, Subash M, Perumal V, Panimalar S, Aravindan S, Uthrakumar R, Inmozhi C, Isaev AB, Muniyasamy S, Raja A, Kaviyarasu K. Specific charge separation of Sn doped MgO nanoparticles for

photocatalytic activity under UV light irradiation. Separation and Purification Technology. 2022 Aug 1;294:121189. https://doi.org/10.1016/j.seppur.2022.121189

[25] Scott T, Zhao H, Deng W, Feng X, Li Y. Photocatalytic degradation of phenol in water under simulated sunlight by an ultrathin MgO coated Ag/TiO_2 nanocomposite. Chemosphere. 2019 Feb 1;216:1-8. https://doi.org/10.1016/j.chemosphere.2018.10.083

[26] Prabhu PS, Kathirvel P, Maruthamani D, Ram SG. Enhanced photocatalytic activity of methylene blue dye by DIFS synthesized pure and Mn doped MgO nanostructures. Optik. 2023 Jul 1;283:170869. https://doi.org/10.1016/j.ijleo.2023.170869

[27] Zheng X, Gou Y, Peng H, Mao Y, Wen J. Nonthermal plasma sulfurized $CuInS_2$/S-doped MgO nanosheets for efficient solar-light photocatalytic degradation of tetracycline. Colloids and Surfaces A: Physicochemical and Engineering Aspects. 2021 Sep 20;625:126900. https://doi.org/10.1016/j.colsurfa.2021.126900

[28] Ratnam MV, Karthikeyan C, Rao KN, Meena V. Magnesium oxide nanoparticles for effective photocatalytic degradation of methyl red dye in aqueous solutions: optimization studies using response surface methodology. Materials Today: Proceedings. 2020 Jan 1;26:2308-13. https://doi.org/10.1016/j.matpr.2020.02.498

[29] Chahar D, Kumar D, Thakur P, Thakur A. Visible light induced photocatalytic degradation of methylene blue dye by using Mg doped Co-Zn nanoferrites. Materials Research Bulletin. 2023 Jun 1;162:112205. https://doi.org/10.1016/j.materresbull.2023.112205

[30] Ali AA, El Fadaly EA, Deraz NM. Auto-combustion fabrication, structural, morphological and photocatalytic activity of CuO/ZnO/MgO nanocomposites. Materials Chemistry and Physics. 2021 Sep 15;270:124762. https://doi.org/10.1016/j.matchemphys.2021.124762

[۳۱] An X, Chen Y, Ao M, Jin Y, Zhan L, Yu B, Wu Z, Jiang P. Sequential photocatalytic degradation of organophosphorus pesticides and recovery of orthophosphate by biochar/α-$Fe_۲O_۳$/MgO composite: A new enhanced strategy for reducing the impacts of organophosphorus from wastewater. Chemical Engineering Journal. 2022 May 1;435:135087. https://doi.org/10.1016/j.cej.2022.135087

[32] Su X, Cao N, Feng J, Li W, Ding X, Li Z, Gao M, Hu L, Zhang H, Ren Y, Wei T. The enhanced photocatalytic performance of the amorphous carbon/MgO nanofibers: Insight into the role of the oxygen vacancies and 1D morphology. Applied Surface Science. 2023 Apr 15;616:156470. https://doi.org/10.1016/j.apsusc.2023.156470

[33] Mylarappa M, Raghavendra N, Surendra BS, Kumar KS, Kantharjau S. Electrochemical, photocatalytic and sensor studies of clay/MgO nanoparticles. Applied Surface Science Advances. 2022 Aug 1;10:100268. https://doi.org/10.1016/j.apsadv.2022.100268

[34] Bateni A, Valizadeh K, Salahshour Y, Behroozi AH, Maleki A. Fabrication and characterization of pectin-graphene oxide-magnesium ferrite-zinc oxide nanocomposite for photocatalytic degradation of diclofenac in an aqueous solution under visible light irradiation. Journal of Environmental Management. 2022 Dec 15;324:116358. https://doi.org/10.1016/j.jenvman.2022.116358

[35] Liu Y, Zhang L, Liu T, Wang J. Photocatalytic selective oxidation of ammonium to dinitrogen by FeOx-MgO activated persulfate under solar-light irradiation. Chemical Engineering Journal. 2023 Feb 15;454:140499. https://doi.org/10.1016/j.cej.2022.140499

[36] Arif S, Nawaz M, Siddique S, Ayub R, Saleem S. Synthesis, characterization and photocatalytic activity of $Mg_{1-x}Cu_xO$ nanoparticles for wastewater treatment. Materials Today Communications. ۲۰۲۲ Dec 1;33:104361. https://doi.org/10.1016/j.mtcomm.2022.104361

[۳۷] Abdollahi B, Farshnama S, Asl EA, Najafidoust A, Sarani M. Cu (BDC) metal–organic framework (MOF)-based Ag_2CrO_4 heterostructure with enhanced solar-light degradation of organic dyes. Inorganic Chemistry Communications. 2022 Apr 1;138:109236. https://doi.org/10.1016/j.inoche.2022.109236

[38] Sadjadi S, Koohestani F. Palladated composite of Cu-BDC MOF and perlite as an efficient catalyst for hydrogenation of nitroarenes. Journal of Molecular Structure. 2022 Feb 15;1250:131793. https://doi.org/10.1016/j.molstruc.2021.131793

[39] Silva BC, Irikura K, Flor JB, Dos Santos RM, Lachgar A, Frem RC, Zanoni MV. Electrochemical preparation of Cu/Cu_2O-Cu (BDC) metal-organic framework electrodes for photoelectrocatalytic reduction of CO_2. Journal of CO_2 Utilization. 2020 Dec 1;42:101299. https://doi.org/10.1016/j.jcou.2020.101299

[40] Alamgholiloo H, Zhang S, Ahadi A, Rostamnia S, Banaei R, Li Z, Liu X, Shokouhimehr M. Synthesis of bimetallic 4-PySI-Pd@ Cu (BDC) via open metal site Cu-MOF: Effect of metal and support of Pd@ Cu-MOFs in H_2 generation from formic acid. Molecular Catalysis. 2019 Apr 1;467:30-7. https://doi.org/10.1016/j.mcat.2019.01.031

[41] Sadjadi S, Koohestani F. Composite of magnetic carbon quantum dot-supported ionic liquid and Cu-BDC (CCDC no. 687690) MOF: A triple catalytic composite for chemical transformations. Journal of Solid State Chemistry. 2022 Apr 1;308:122888. https://doi.org/10.1016/j.jssc.2022.122888

[42] Zhao L, Xia W. Stainless steel membrane UF coupled with NF process for the recovery of sodium hydroxide from alkaline wastewater in chitin processing. Desalination. 2009 Dec 15;249(2):774-80. https://doi.org/10.1016/j.desal.2009.01.036

[43] Nasr Esfahani K, Farhadian M, Solaimany Nazar AR. Interaction effects of various reaction parameters on the treatment of sulfidic spent caustic through electro-photo-Fenton. International Journal of Environmental Science and Technology. 2019 Nov;16:7165-74. https://doi.org/10.1007/s13762-018-2126-8

[44] Mosleh S, Khaksar H. Cu-BDC MOF/CNFs hybrids for rapid CO_2 capture in a circulating fluidized bed via temperature swing adsorption process. Chemical Engineering Science. 2024 Apr 5;287:119773. https://doi.org/10.1016/j.ces.2024.119773

[45] Hasan IF, Basim HS, Ibrahim RK, Saadoon NM, Saadoon MM. Effect of MgO-NPs on the Morphology and Function of Kidney in Male Albino Mice. Journal of Nanostructures. 2025 Oct 1;15(4):1690-9. DOI: 10.22052/JNS.2025.04.016

[46] American Public Health Association. APHA standard methods for the examination of water and wastewater. Standard methods for the examination of water & wastewater. Washington, DC: American Public Health Association. 2005.

[47] Sadjadi S, Koohestani F. Palladated composite of Cu-BDC MOF and perlite as an efficient catalyst for hydrogenation of nitroarenes. Journal of Molecular Structure. 2022 Feb 15;1250:131793. https://doi.org/10.1016/j.molstruc.2021.131793.

[٤٨] Li Z, Xia H, Li S, Pang J, Zhu W, Jiang Y. In situ hybridization of enzymes and their metal–organic framework analogues with enhanced activity and stability by biomimetic mineralisation. Nanoscale. 2017;9(40):15298-302. https://doi.org/10.1039/C7NR06315F.

[49] James MS, Garg A. Performance of electro-Fenton process for the treatment of synthetic sulphidic spent caustic waste stream generated from petroleum refineries. Chemosphere. 2024 Jan 1;346:140572. https://doi.org/10.1016/j.chemosphere.2023.140572.